PhotoniX

Vacuum-ultraviolet (λ < 200 nm) photodetector array

Siqi Zhu[1†], Zhuogeng Lin[1†], Zhao Wang[1], Lemin Jia[1], Naiji Zhang[1] and Wei Zheng[1*]

[†]Siqi Zhu and Zhuogeng Lin contributed equally to this work.

*Correspondence:
zhengw37@mail.sysu.edu.cn

[1] State Key Laboratory of Optoelectronic Materials and Technologies, School of Materials, Sun Yat-Sen University, Shenzhen 518107, China

Abstract

The vacuum-ultraviolet (VUV, 10–200 nm) imaging photodetector (PD) based on the wide bandgap semiconductor (WBGS) can realize a more detailed observation of solar storms than the silicon ones. Here, an 8×8 VUV PD array based on the semiconductor AlN with an ultra-wide bandgap is presented, exhibiting the shortest cutoff wavelength (203 nm) reported so far. The PD array with a Pt/AlN/SiC/Ti/Au photovoltaic structure shows an excellent selective response to VUV light, an extremely low dark current density of 2.85×10^{-11} A·cm^{-2}@ -2 V, a responsivity of 0.054 A·W^{-1}@ 0 V and an ultra-short rise time of 13 ns. Also, the clear boundaries and an obvious contrast between light and dark of the VUV image displayed in the imaging measurement indicate the good imaging ability of this PD array, which can be used for the imaging application with high signal-to-noise ratio and high response speed. These results provide rich experience for the development of VUV imaging PDs based on WBGSs both in their fabrication and the practical applications in VUV detection.

Keywords: Vacuum-ultraviolet detection, Photodetector array, Wide bandgap semiconductors, Imaging

Introduction

The sun not only affects the weather and climate of Earth but also acts as the main trigger for space weather phenomena. The emission phenomena (solar storms) such as coronal mass ejections and solar flares from the sun will cause ionospheric disturbances and magnetic storms on Earth, which may lead to huge economic losses [1–4]. Therefore, a real-time monitoring of solar activity is necessary for the prediction of disastrous space weather events. Vacuum-ultraviolet (VUV) light is in the range of 10–200 nm [5]. VUV imaging detection with an extremely low solar background noise is an effective means to monitor solar activity [6–8]. The monitoring scenario of VUV imaging photodetectors (PDs) for solar storms is shown in Fig. 1a.

In the field of VUV detection, the PDs mainly used are based on the photomultiplier tube and silicon photodiodes, but both are faced with some shortcomings hindering further development [9]. For the photomultiplier tube, the large gain and high sensitivity are unable to cover the problems of high energy consumption and low-temperature conditions. In comparison, semiconductors are more suitable to be the materials for VUV PDs. However, the silicon semiconductor PDs need a filter system with complex
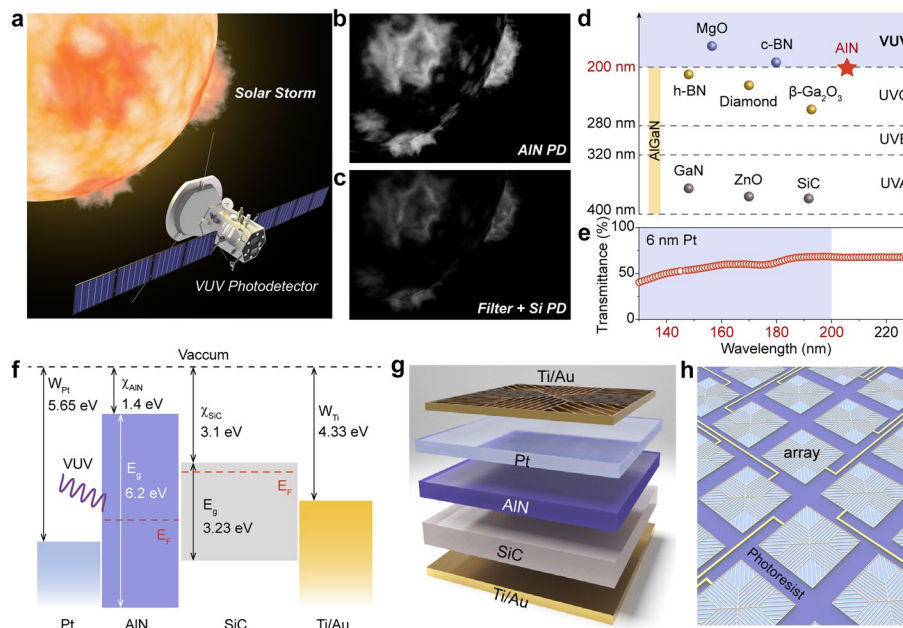
Fig. 1 Application of VUV imaging detection and the designed structure of the VUV PD array. **a** Solar storm detection by the VUV PD array. The imaging schematic diagram of **b** a WBGS PD (using AlN as an example) and **c** a silicon PD with a filter added. **d** Distribution of the ultraviolet spectrum and bandgap of common WBGSs. **e** Transmittance of 6 nm Pt metal in the range of 130~230 nm. **f** Band structure of the designed AlN-based photovoltaic PD (Pt/AlN/SiC/Ti/Au, pre-contact). **g** Single pixel and **h** array structure diagram of the AlN-based PD array

structure to remove visible light interference, causing a loss of many weak signals. In addition, silicon PDs have poor radiation resistance, which may result in degradation and failure of device performance. Therefore, researchers have been committed to exploring the new VUV PDs. Starting from this demand, PDs based on wide-bandgap semiconductors (WBGSs) are considered as a new generation of VUV PDs due to the advantages of low operating voltage, good spectral selectivity and excellent radiation resistance [5, 10, 11]. The WBGS PDs complete a more effective observation of the characteristics of solar storms without any additional filters, which can capture the weak signals to lower the risk of losing details (Fig. 1b and c). However, compared with the visible and infrared imaging PDs which has been commercially available, the ultraviolet PDs dependent on WBGSs is still on the level of scientific research with the focus put on prototype single point devices.

The typical WBGSs can be found in Fig. 1d, such as gallium oxide (Ga_2O_3) [12–14], diamond [15], hexagonal boron nitride (h-BN) [16] and AlGaN [17–19]. Among them, aluminum nitride (AlN) has an ultra-wide direct bandgap of 6.2 eV, which exactly corresponds to the long wavelength limit of 200 nm in the VUV band. This characteristic makes it a great candidate material for unfiltered VUV detectors. In addition, AlN has the advantages such as superior radiation resistance, and high chemical and thermal stability [20–24], able to meet the detection needs in extreme space environments. In previous research, we have successfully prepared the single-point and line-array devices of AlN-based VUV PDs [6, 25–29], achieving ideal responsivity and extremely fast response. On this basis, in this work, we have constructed an 8×8 VUV PD array with

a photovoltaic structure of Pt/AlN/SiC/Ti/Au, exhibiting excellent photoelectric performance. The manufacturing of the 8×8 PD array adopts a multi-step lithography process with no etching required. This work is expected to promote the practical applications of the new-generation VUV imaging PD based on WBGSs.

Results and discussion

Structural design of the AlN-based VUV photodetector array

A good PD array needs to ensure that its pixels have a good photoelectric performance. At present, most of the reported shortwave ultraviolet PD arrays based on WBGSs have a photoconductive structure [30–34] whose manufacturing process is relatively simple. Although it can achieve an ultra-high responsivity through the gain mechanism, the long relaxation time of non-equilibrium carriers will lead to a long response time of the device and it requires external bias operation during that process. Compared with photoconductive ones, photovoltaic PDs have the advantages of low dark current, high response speed and no need for external bias voltage due to the existence of a built-in electric field [35]. Therefore, a VUV PD array based on the AlN thin film with a photovoltaic structure was designed here, which should consider the following points.

First, the substrate of AlN film should be well matched with the lattice constant and the thermal expansion coefficient of AlN (At present, the AlN single crystal cannot achieve the arbitrary regulation of carrier concentration, so it cannot be applied for homoepitaxy), so high-quality silicon carbide (SiC) single crystals were chosen as the substrate, with the conductive n-type SiC selected to construct larger internal electric fields. Besides, the upper electrode should be able to transmit VUV light and its Fermi level should be much lower than that of AlN for a high open circuit voltage. Based on that, the platinum (Pt) metal with a high transmittance to VUV light and the highest work function was chosen here. The transmittance of 6 nm Pt electrode to VUV light has been measured as approximately 55% from 130 to 200 nm, as shown in Fig. 1e. Thus, Pt can be used as a semi-transparent electrode to ensure that most of the VUV light irradiating on the device can be absorbed by the AlN photosensitive layer. Lastly, Ti/Au metal was selected as the bottom electrode to contact SiC because it has good adhesion and with no hindrance to carrier transmission. The band structure of this designed Pt/AlN/SiC/Ti/Au device (pre-contact) is shown in Fig. 1f.

Based on that device structure, the schematic diagrams of one single pixel and array of the AlN-based VUV PD array are shown in Fig. 1g and h. The electrodes of the PD array are designed as 8×8 anodes (top electrode) and one common cathode (bottom electrode) through a multi-step lithography without etching. To improve the efficiency of collecting photo-generated carriers, the photosensitive array pixels were covered with fine grid metal; to reduce crosstalk, a photoresist unable to transmit VUV light was used to cover the non-photosensitive positions of the AlN film to prevent the absorption of VUV light.

Fabrication of the AlN-based VUV photodetector

Figure 2a shows the fabrication process of the AlN-based 8×8 PD array, which mainly involves photolithography and electrode plating. The fabricated process of PD array does not require etching, which can improve the fabrication efficiency and
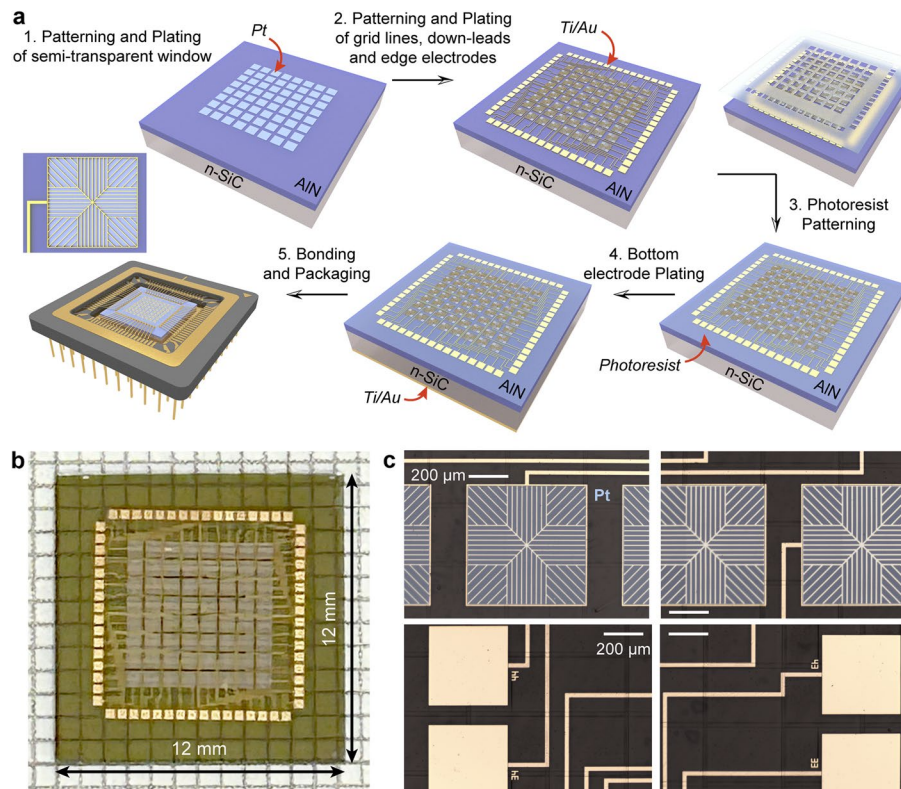
Fig. 2 Fabrication of the AlN-based 8 × 8 VUV PD array. **a** Device fabrication process, which is divided into five steps. Step 1 is the patterning and plating of the semi-transparent window Pt electrode; Step 2 is the patterning and plating of grid lines, down-leads and edge electrodes; Step 3 is the photoresist patterning to cover the non-photosensitive region; Step 4 is the bottom electrode plating; Step 5 should be the bonding and packaging of the PD array. **b** Photograph and **c** microscopic images of the AlN PD array. Since Pt electrodes are too transparent to be observed, the Pt electrode regions are marked by blue squares

accuracy of the device. Firstly, 8 × 8 Pt electrodes were plated on the surface of AlN/SiC wafer by photolithography and ion sputtering (Step 1). The electrode size of a single pixel was 600 × 600 µm, and the width between electrodes was 200 µm. Secondly, through overlap and electron beam evaporation, both down-lead in contact with Pt electrodes and edge electrodes were formed for subsequent packaging, and the pixels were covered with grid metal lines to improve the collection efficiency of photo-generated carriers (Step 2). The metal used was Ti/Au (10/100 nm), with each down-lead width of 20 µm, grid line width of 5 µm and the edge electrode size of 400 × 400 µm. Thirdly, the photoresist was used to cover the area outside the photo-sensitive array and the edge electrodes (Step 3) so that only the photosensitive array can respond to VUV light. The edge electrodes were thick Ti/Au metals that VUV light cannot pass through. Then, Ti/Au (10/100 nm) was obtained by hot evaporation plating on the back of the SiC substrate, used as the common cathode (bottom electrode) of the PD array (Step 4). Finally, the device electrodes should be bonded into the ceramic pin grid array packaging shell for packaging (Step 5). Figure 2b and c show the photograph and microscope images of the fabricated PD array, where the clear electrode images illustrates that the fabrication process is reliable. The two digits near the edge electrodes represent the position of connected array pixels, with the

first digit representing the row and the second digit representing the column, facilitating subsequent packaging and readout circuit connections.

Characterizations of the AlN-based VUV photodetector array

In the process of device fabrication, a series of characterizations have been conducted on the AlN film, photoresist and Pt metal. For a PD, the high-quality optical absorption layer is a prerequisite to ensure a good photoelectric performance, which can reduce the recombination caused by defects and thus facilitates the separation and migration of photogenerated carriers. Figure 3a and b show the low-magnification and high-resolution transmission electron microscopy (TEM) images as well as the diffraction images of AlN/SiC heterojunction cross sections. The AlN film is extremely flat with a thickness of about 219.7 nm and a good crystal orientation. Figure 3c shows the Raman spectrum of AlN/SiC wafer, from which a typical E_2^{high} phonon mode of AlN can be observed, reflecting its good crystal quality. The frequency of E_2^{high} mode can be applied to estimate the strain in the AlN epilayer considering the frequency of strain-free AlN is 656 cm^{-1} [36]. The measured E_2^{high} mode is at 657.4 cm^{-1} indicating a compressive strain around 0.28 GPa [37]. Furthermore, the X-ray diffraction (XRD) rocking curve of the (0002) crystal face of the AlN film exhibits a good crystallization quality, with a full width at half maximum of 350 arcsec, as shown in Fig. 3d. In addition, according to the photoluminescence (PL) spectrum of
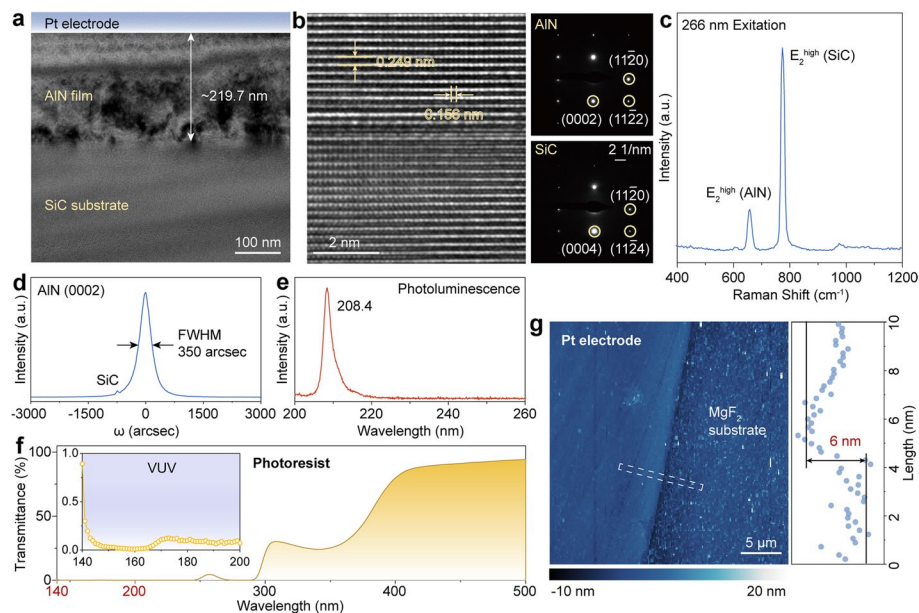

Fig. 3 Characterization of the AlN-based VUV PD array. Cross section **a** low-magnification TEM image and **b** high-resolution TEM image and diffraction images of the AlN/SiC heterojunction. **c** Raman spectrum of AlN/SiC wafer excited by a 266 nm laser. **d** Rocking XRD curve of the (0002) crystal face of the AlN film. The small peak to the left of the main peak is the (0004) diffraction peak of SiC. Due to the similar diffraction peak angles of AlN and SiC, the SiC diffraction peak cannot be filtered out completely. **e** PL spectrum of the AlN film. **f** Transmittance of the photoresist used for the fabrication of the PD array in the range of 140~500 nm. The insert shows the transmittance in the VUV range (140~200 nm). **g** AFM image of the Pt electrode. The Pt electrode has a thickness of about 6 nm

the AlN film shown in Fig. 3e, the band edge emission with the central wavelength of the luminescence peak of 208.4 nm can be clearly observed without defects emission.

The transmittance of the photoresist to VUV light was also measured, as exhibited in Fig. 3f. The photoresist used in the device is completely opaque to 140–200 nm light, so the non-pixel AlN film cannot absorb VUV light. Further, the thickness of the Pt metal electrode was characterized through atomic force microscopy (AFM), as shown in Fig. 3g, based on which the thickness of Pt electrode is around 6 nm. These results further demonstrate the structural feasibility of the PD array.

Photoelectric performance of the AlN-based VUV photodetector array

VUV photoelectric measurements were conducted on a single pixel of the fabricated PD array, as shown in Figs. 4 and 5. Figure 4a shows the J-V curves of a single pixel device under 185 nm (334.2 $\mu W \cdot cm^{-2}$) light illumination and in the dark. The ultra-low dark current density (J_{dark}) (2.85×10^{-11} A·cm^{-2} @-2 V) indicates a high resistance of the AlN photosensitive layer (The area involved in dark current is approximately 0.52 mm^2). It is worth noting that J_{dark} should be zero at ideal 0 V bias. The measured dark current at 0 V is not the true value, which is related to the source meter. The ratio of photocurrent density to dark current density (J_{photo}/J_{dark}) of the device at reverse bias is about 6 orders of magnitude, illustrating that the device should have a high signal-to-noise ratio. In addition, due to the designed structure, the single pixel device also has a high open circuit voltage (V_{oc}) of 1.9 V, which can operate in an environment without any external input. This high voltage displayed by the device after overcoming the internal resistance comes from the difference of the large Fermi level between Pt and SiC [27]. Figure 4b shows the J-V curves under different light power densities. With the increase of light power density, both the photocurrent and the open circuit voltage of the single pixel device increase. Figure 4c shows the multi-period J-T curves at 0 V, -2 V, and -5 V (For
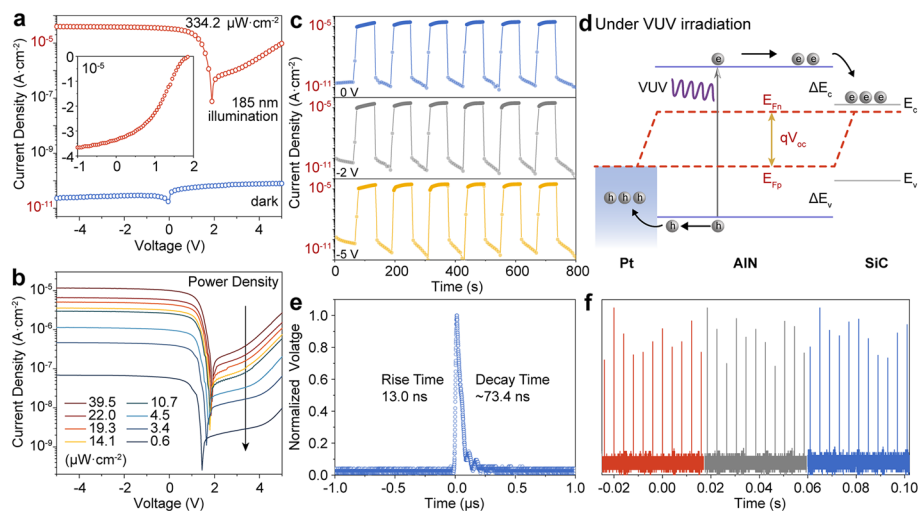

Fig. 4 Photoelectric performance of one single pixel device of the AlN-based VUV PD array. **a** J-V curves under 185 nm monochromatic light (334.2 $\mu W \cdot cm^{-2}$) and in the dark. **b** J-V curves under the condition of different power densities (0.6 ~ 39.5 $\mu W \cdot cm^{-2}$) of 185 nm light. **c** Multi-period J-T curves of 0 V, -2 V and -5 V under 185 nm light illumination. **d** Band structure diagram of the device under VUV illumination. **e** 193 nm single pulse response curve. The rise time and decay time are 13.0 ns and 73.4 ns, respectively. **f** 193 nm multi-pulse response curve
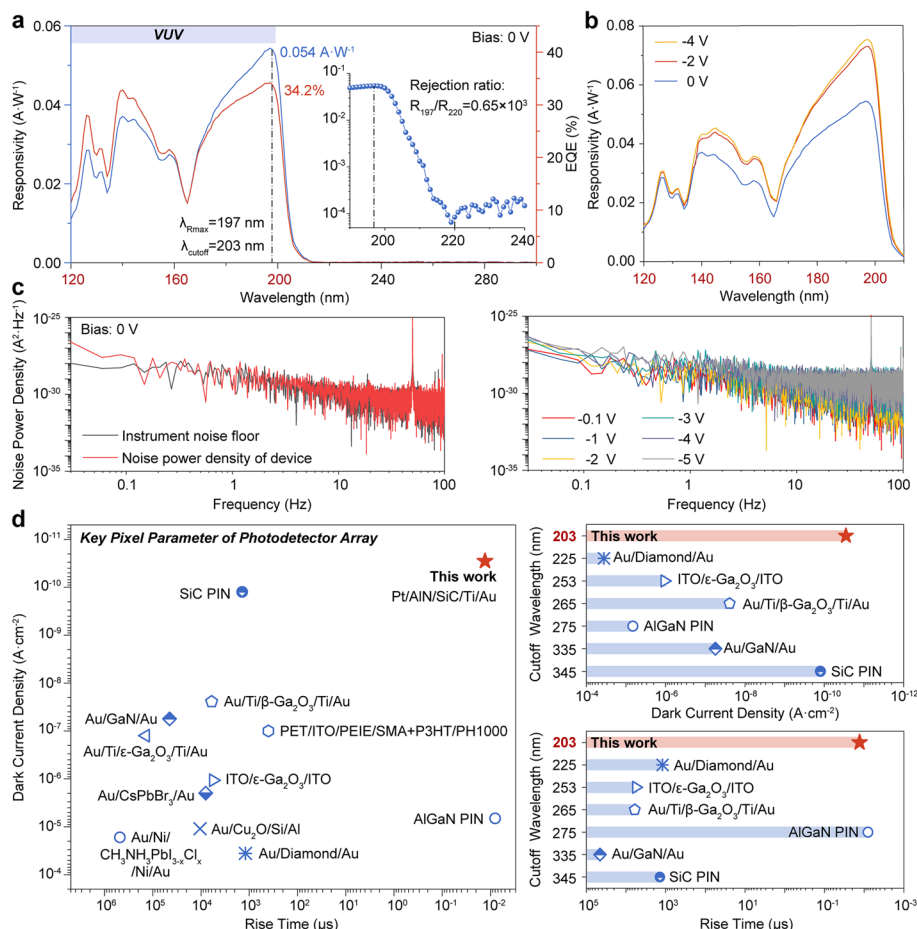
Fig. 5 Photoelectric performance of one single pixel device of the AlN-based VUV PD array and the performance comparison. **a** Responsivity and EQE curves at 0 V bias in the range of 120 ~ 300 nm. The insert shows the vertical coordinates of responsivity as logarithms. **b** Spectral responsivity curves at different bias voltages. **c** Low-frequency noise power spectral density at open circuit and connected state with 0 V and reverse bias. **d** Comparison of cutoff wavelength, dark current density and rise time of the reported UV PD arrays. Ref [38]: SiC PIN; Ref [39]: PET/ITO/PEIE/SMA + P3HT/PH1000; Ref [30]: Au/Ti/β-Ga$_2$O$_3$/Ti/Au; Ref [40]: Au/GaN/Au; Ref [41]: Au/Ti/ε-Ga$_2$O$_3$/Ti/Au; Ref [32]: ITO/ε-Ga$_2$O$_3$/ITO; Ref [42]: Au/CsPbBr$_3$/Au; Ref [43]: Au/Cu$_2$O/Si/Al; Ref [31]: Au/Diamond/Au; Ref [44]: Au/Ni/CH$_3$NH$_3$PbI$_{3-x}$Cl$_x$/Ni/Au; Ref [45]: AlGaN PIN

convenience, the area used for calculating J$_{photo}$ and J$_{dark}$ is both 0.36 mm^2). The J$_{photo}$/J$_{dark}$ under different bias voltages is similar, stable, and repeatable, indicating a reliable operation of the device. Figure 4d is the band structure diagram of the device during operation (The band structure diagram in equilibrium state is shown in Supplementary Fig. 1). Through the semi-transparent Pt window, VUV light irradiates on the AlN film to produce photogenerated electron–hole pairs. Electrons and holes are separated with the electrons migrating to the SiC direction and the holes to the Pt direction under the action of an internal electric field. Therefore, the Pt/AlN/SiC/Ti/Au structure designed in this work can also be regarded as a PIN type.

Then, the response speed of the single pixel device was tested. Time response test methods can be found in the Method Section and Supplementary Information (Supplementary Figs. 2–6 and Supplementary Table 1). Figure 4e and f are the results of 193 nm

pulse response test. With a rising edge of about 13.0 ns and a falling edge of 73.4 ns, this device can meet the requirement for fast response. In addition, under the illumination of multiple light pulses, the device shows a stable output voltage. The fluctuation of the output voltage is due to the instability of the incident laser intensity, which can be demonstrated by the multi-pulse response curve of commercial silicon PD (Supplementary Fig. 6).

Figure 5a shows the responsivity (R) and external quantum efficiency (EQE) of the single pixel device at 0 V bias from VUV to deep-UV (120–300 nm), with $R = \frac{I_{photo} - I_{dark}}{PS}$ and $EQE = \frac{hcR}{q\lambda} \times 100\%$ (P is the light power density, S is the photosensitive area of the device, h is the Planck's constant, c is the speed of light, q is the electron charge and λ is the measured wavelength.) [46, 47]. The cutoff wavelength of the device is 203 nm, indicating a good selective response to VUV light, which corresponds to the PL spectrum of the AlN film (Fig. 3e). The largest response is exhibited at 197 nm, with R of 0.054 A·W^{-1} and EQE of 34.2%. In fact, considering the reflection of light by the grating metal on the photosensitive pixel, the actual R and EQE should be larger than these values. The VUV spectral responsivity curves under different reverse bias voltages are shown in Fig. 5b. In the case of external reverse bias, the spectral response curve is similar, and the responsivity shows a slight increase. The specific detectivity (D*) of the photodetector shows about 2.2×10^{13} Jones with $D^* = \frac{R}{\sqrt{2eJ_{dark}}}$ (197 nm, -2 V). Compared with many photovoltaic PDs, our PD shows a higher specific detectivity due to the ultra-low dark current density.

In addition, noise control is considered as one of the most important factors for the operation of PDs. Figure 5c shows the noise power spectral density of the single pixel device at 0.03–100 Hz. Compared to the background noise, the noise captured as the device has been connected to the circuit system just changed a little. At 0 V, the noise power density of the device is lower than 10^{-25} A^2·Hz^{-1}, which is almost the same under reverse bias, indicating a very low noise level possessed by this device. Another pixel device has been chosen to repeat the photoelectric test, and the results are similar to those in Figs. 4 and 5, as shown in Supplementary Figs. 7–9. Figure 5d and Supplementary Table 2 show the UV PD arrays reported so far, comparing their device structures and photoelectric performance. The PD array fabricated in this work has the shortest cut-off wavelength, a much lower dark current density, and a shorter rising time. Regarding the deep ultraviolet detection, AlGaN PD arrays are more mature, which can achieve more pixels with excellent photoelectric performance [48]. The rise time of the device is close to the reported result of AlGaN, and the dark current density is much lower [45]. The responsivity and EQE of the device have room for improvement.

The response uniformity of pixels is a prerequisite for high-performance imaging. To figure out the difference in photoelectric performance of each pixel device, the J-V curves of 64 pixel devices were tested under the same illumination conditions (185 nm, 334.2 μW·cm^{-2}). Figure 6a and b show the J_{photo} value distribution and the mapping of those pixel devices under -4 V and 0 V bias, and Supplementary Fig. 10 exhibits the J_{photo}-V curves of the pixel devices in lines 4 and 8. For the 64 pixel devices, there are no bad spots and the J_{photo} is evenly distributed. It is worth noting that since the 185 nm light is non-parallel, the fluctuations of J_{photo} are partly caused by the uneven regional light sources. At 0 V bias, J_{photo} fluctuates in the range of 93–122 nA with a stable
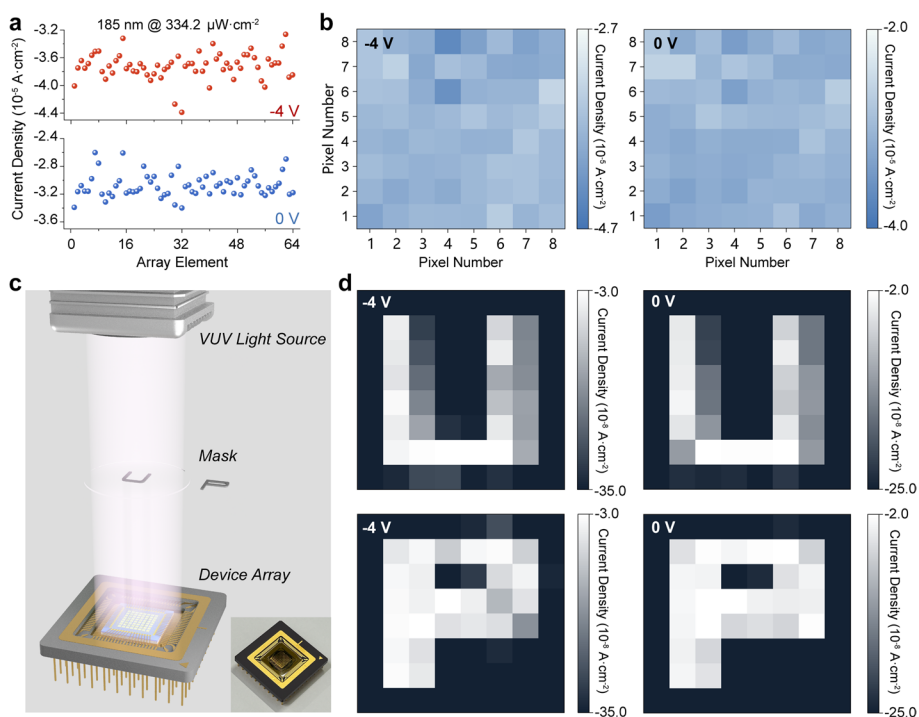
Fig. 6 Uniformity and imaging tests of the AlN-based VUV PD array. **a** J_{photo} value distribution and **b** the J_{photo} mapping at -4 V and 0 V bias under 185 nm light illumination. **c** Schematic diagram of the optical path of the imaging test. The insert is a photograph of the PD array. **d** VUV imaging results at -4 V and 0 V bias

consistency. The mean value of J_{photo} is 111 nA with a maximum standard deviation of 9.9% (($J_{photo, max}$-$J_{photo, ave}$)/$J_{photo, ave}$). These results both demonstrate the uniformity of these devices and indirectly show the uniformity of AlN thin films as well as the feasibility and reliability of the device design and manufacturing scheme.

Lastly, the imaging ability of the AlN-based VUV PD array was tested. With an EQ-99X LDLS wide spectrum light source as the VUV light source, a sapphire mask with the designed pattern ("U "and "P") was imaged. The optical path built for this imaging test is shown in Fig. 6c, in which the light source, mask, and PD array were placed in the same straight line. Under VUV illumination, the areas outside this imaging pattern allowed light to pass through and reach the PD array, resulting in the pattern area being in a dark state and the remaining areas being illuminated. It is worth noting that due to the reflection of the metal inside the vacuum chamber, there was still some light absorption in the pattern area. Figure 6d shows the VUV imaging mappings of "U "and "P" under -4 V and 0 V bias, from which the VUV images are observed to have clear boundaries, an obvious contrast between light and dark, and a very high similarity to the physical image. This result indicates that the VUV PD array has a high fidelity, which is promising to be applied in practical VUV detection.

Although the PD array reported here only has 64 pixels, this is the new try of VUV imaging through the PDs based on WBGSs to the best of our knowledge (Supplementary Table 2). Future study will focus on the increase of device pixels and the construction of matching readout circuits to develop a full-chain VUV imaging system based on WBGSs. Overall, this work is just the beginning but expected to effectively promote the

VUV imaging detection based on WBGSs in real applications, especially for the solar storm monitoring.

Conclusions

In conclusion, an 8×8 unfiltered VUV PD array based on the WBGS was reported. The PD array with a Pt/AlN/SiC/Ti/Au photovoltaic structure has a good selective response to VUV light, exhibiting an extremely low dark current (2.85×10^{-11} A·cm^{-2} @ -2 V), a high responsivity (0.054 A·W^{-1} @ 0 V), and a high response speed (13 ns). The PD array was obtained by the multi-step lithography without etching. Based on the imaged VUV graphics with clear boundaries, clear contrast between light and dark, and high similarity to the actual image, the PD array has been demonstrated to possess a good imaging ability. This work is expected to provide experience for the fabrication of VUV imaging PDs based on WBGSs and promote their practical applications in solar storm monitoring.

Methods

Materials characterization

AlN films were obtained by heteroepitaxial growth on a 2-inch n-SiC single crystal substrate through the metal–organic chemical vapor deposition, with the epitaxial temperature and pressure respectively set at 200 Torr and 1050 ℃, trimethyl aluminum and ammonia taken as the aluminum and nitrogen sources, and hydrogen used as the carrier gas. TEM images of AlN/SiC heterostructure cross sections were captured by FEI Talos F200 S Transmission electron microscopy. The rocking XRD curve of AlN thin films was measured by Panalytical Empyrean-Xpert Pro MPD X-ray diffractometer. The PL spectrum was obtained by the excitation of EX5/250 ArF excimer laser (193 nm) and the collection of the QE65PRO scientific spectrometer with H70 grating. The Raman spectrum was measured using a Renishaw spectrometer (inVia Reflex) excited by a 266 nm laser. The transmittance of the Pt metal and the photoresist to VUV light was measured using a self-built VUV spectroscopy system. The Pt metal was plated on a MgF$_2$ substrate through the same process used in the device preparation (with the MgF$_2$ substrate as the background). The photoresist was applied on a sapphire substrate through the same process used in the device preparation (with the sapphire substrate as the background). The AFM image of Pt metal was acquired by AIST Smart SPM Scanning Probe Microscope of Horiba France SAS Company.

Device fabrication

First, the AlN/SiC wafer was cut into 12×12 cm sized pieces by laser cutting to fabricate the PD arrays. Then, 8×8 PD arrays were fabricated on the piece through multi-step photolithography and plating electrodes process. Negative photoresist was used, model AZ2035. The photoresist exposure was performed by Heidelberg's µPG501 laser direct writing lithography system. After that, Pt electrode was plated by Quorum's Q150 ion sputtering meter. The Ti/Au grid lines, down-leads and edge electrodes were fabricated through DE400 electron beam evaporation from Wevetest. The Ti/Au electrode at the bottom of SiC substrate was plated by JSD350 thermal evaporation system of Anhui Jiashuo Company.

Photoelectric measurements

The I-V and I-T curves of the array devices in the vacuum chamber were measured by Keithley 4200A-SCS source meter. The VUV light source was provided by a low-pressure mercury lamp (185 nm Monochromatic light). Different light powers were obtained by adding attenuation plates with different attenuation coefficients on the optical path. The light power density was calibrated by the commercial standard Si PD (AXUV20A, from Opto Diode Company). The measurement of device noise characteristics was conducted in vacuum. First, the dark current of the device was sampled and digitized by Keithley 2636B source meter in the time domain. Then, the noise power spectral density in the frequency domain was obtained by Fourier transform.

A self-assembled vacuum spectral response testing system was applied to measure the spectral responsivity, which includes a L11798 (Hamamatsu) 200 W deuterium lamp, a McPherson 302 monochromator, a micro probe station which is placed in a vacuum chamber, and a Keithley 6517B/2636B source meter. In a vacuum state, a continuous deuterium lamp light source was split through a monochromator, with the light irradiating on the pixel device of the PD array. The electrical signal was then led to the source meter through a probe for reading.

The pulse response test was conducted through the self-assembled VUV pulse response test system, which includes an EX5/250 ArF excimer laser (193 nm), a micro probe station, and an SDS5104X SIGLENT digital storage oscilloscope. Through the established optical path, the 193 nm laser irradiated to the pixel device, and then the electrical signal was led to the oscilloscope through the probe for reading. More detailed information of the test circuit was shown in the Supplementary Information (Supplementary Figs. 2–6 and Supplementary Table 1).

The VUV light source used for the imaging measurement was provided by the EQ-99X LDLS lamp. The imaging patterns came from the sapphire mask. During the test, the light source, mask, and PD array were placed in the same straight line. With the I-V curve of each array pixel recorded point by point, the photocurrent value could be converted into a hot spot map to present the VUV imaging results.

Abbreviations

VUV	Vacuum-ultraviolet
PD	Photodetector
WBGS	Wide bandgap semiconductor
AlN	Aluminum nitride
TEM	Transmission electron microscopy
XRD	X-ray diffraction
AFM	Atomic force microscopy
PL	Photoluminescence
J_{dark}	Dark current density
J_{photo}	Photocurrent density
R	Responsivity
EQE	External quantum efficiency

Supplementary Information

The online version contains supplementary material available at https://doi.org/10.1186/s43074-024-00120-z.

Additional file 1: Supplementary Fig. 1. Energy band diagram of the photodetector in equilibrium state. Pulse Response Testing Circuit Description. **Supplementary Fig. 2.** Pulse response testing circuit of the photodetector. **Supplementary Fig. 3.** a Equivalent circuit diagram of the pulse response test in previous work. The device was connected in series with a sampling resistor R_L, and the impedance of the oscilloscope was set to 1 MΩ. b Pulse

response curves of a single pixel device in the AlN PD array with different sampling resistors R_L in the high impedance test. The higher the R_L, the longer the response time of the device. **Supplementary Table 1.** The rise time and decay time of a single pixel device in the AlN PD array tested under different sampling resistors R_L with high impedance. **Supplementary Fig. 4.** Fitting result of the pulse response curve using equation (S1) with $R_L = 1\ G\Omega$. **Supplementary Fig. 5.** a Equivalent circuit diagram of the pulse response test in this work. The coaxial cable connecting the device to the oscilloscope has an impedance of 50 Ω, and the impedance of the oscilloscope is set to 50 Ω. b Pulse response curve of a single pixel device in the AlN PD array in the low impedance test. **Supplementary Fig. 6.** a Pulse response curve of the silicon PD in the low impedance test, with the rise time of about 26.8 ns and the decay time of around 6.9 μs. b Multi-pulse response curve of the silicon PD in the low impedance test. **Supplementary Fig. 7.** a J-V curves of another pixel device under 185 nm monochromatic light (334.2 μW·cm^{-2}) and in the dark. b J-V curves of another pixel device under the condition of different power densities (0.6 ～ 39.5 μW·cm^{-2}) of 185 nm light. **Supplementary Fig. 8.** Multi-period J-T curves of 0 V, -2 V and -5 V of another pixel device under 185 nm light irradiation. **Supplementary Fig. 9.** Low-frequency noise power spectral spectrum at open circuit and connected state with 0 V and reverse bias of another pixel device. **Supplementary Fig. 10.** J-V curves of the pixel devices in lines a 4 and b 8 under 185 nm monochromatic light (334.2 μW·cm^{-2}). **Supplementary Table 2.** Summary of photoelectric performance of the reported UV PD arrays.

Availability of data and materials
The relevant data of this study are available from the corresponding authors on reasonable request.

Declarations

Competing interests
The authors declare that they have no competing interests.

References
1. Baker DN. How to cope with space weather. Science. 2002;297:1486–7.
2. Cane HV, Richardson IG. Interplanetary coronal mass ejections in the near-Earth solar wind during 1996–2002. J Geophys Res. 2003;108:1156.
3. Temmer M. Space weather: the solar perspective. Living Rev Sol Phys. 2021;18:4.
4. Chamberlin PC, Woods TN, Eparvier FG. Flare Irradiance Spectral Model (FISM): flare component algorithms and results. Space Weather. 2008;6:S05001.
5. Jia L, Zheng W, Huang F. Vacuum-ultraviolet photodetectors. PhotoniX. 2020;1:22.
6. Zheng W, Lin R, Jia L, Huang F. Vacuum ultraviolet photovoltaic arrays. Photonics Res. 2018;7:98–102.
7. Benmoussa A, Dammasch IE, Hochedez JF, Schühle U, Koller S, Stockman Y, et al. Pre-flight calibration of LYRA, the solar VUV radiometer on board PROBA2. Astron Astrophys. 2009;508:1085–94.
8. Liu C, Eschen W, Loetgering L, Penagos Molina DS, Klas R, Iliou A, et al. Visualizing the ultra-structure of microorganisms using table-top extreme ultraviolet imaging. PhotoniX. 2023;4:6.
9. Li Z, Yan T, Fang X. Low-dimensional wide-bandgap semiconductors for UV photodetectors. Nat Rev Mater. 2023;8:587–603.
10. Zheng W, Jia L, Huang F. Vacuum-ultraviolet photon detections. iScience. 2020;23:101145.
11. Yang J, Liu K, Chen X, Shen D. Recent advances in optoelectronic and microelectronic devices based on ultrawide-bandgap semiconductors. Prog Quantum Electron. 2022;83:100397.
12. Wu C, Wu F, Hu H, Wang S, Liu A, Guo D. Review of self-powered solar-blind photodetectors based on Ga2O3. Mater Today Phys. 2022;28:100883.
13. Cheng Y, Ye J, Lai L, Fang S, Guo D. Ambipolarity regulation of deep-UV photocurrent by controlling crystalline phases in Ga2O3 nanostructure for switchable logic applications. Adv Electron Mater. 2023;9:2201216.

14. He H, Wu C, Hu H, Wang S, Zhang F, Guo D, et al. Bandgap engineering and oxygen vacancy defect electroactivity inhibition in highly crystalline N-Alloyed Ga2O3 films through plasma-enhanced technology. J Phys Chem Lett. 2023;14:6444–50.

15. Lu YJ, Lin CN, Shan CX. Optoelectronic diamond: growth, properties, and photodetection applications. Adv Opt Mater. 2018;6:1800359.

16. Moon S, Kim J, Park J, Im S, Kim J, Hwang I, et al. Hexagonal boron nitride for next-generation photonics and electronics. Adv Mater. 2023;35:2204161.

17. Zhang H, Liang F, Song K, Xing C, Wang D, Yu H, et al. Demonstration of AlGaN/GaN-based ultraviolet phototransistor with a record high responsivity over 3.6 × 107 A/W. Appl Phys Lett. 2021;118:242105.

18. Wang D, Liu X, Kang Y, Wang X, Wu Y, Fang S, et al. Bidirectional photocurrent in p–n heterojunction nanowires. Nat Electron. 2021;4:645–52.

19. Wang D, Wu W, Fang S, Kang Y, Wang X, Hu W, et al. Observation of polarity-switchable photoconductivity in III-nitride/MoSx core-shell nanowires. Light Sci Appl. 2022;11:227.

20. Abid A, Bensalem R, Sealy B. The thermal stability of AlN. J Mater Sci. 1986;21:1301–4.

21. Dukenbayev K, Kozlovskiy A, Korolkov I, Zdorovets M. Investigation of radiation resistance of AlN ceramics. Vacuum. 2019;159:144–51.

22. Cheng Z, Koh YR, Mamun A, Shi J, Bai T, Huynh K, et al. Experimental observation of high intrinsic thermal conductivity of AlN. Phys Rev Mater. 2020;4:044602.

23. Yu R, Liu G, Wang G, Chen C, Xu M, Zhou H, et al. Ultrawide-bandgap semiconductor AlN crystals: growth and applications. J Mater Chem C. 2021;9:1852–73.

24. Benmoussa A, Soltani A, Gerbedoen JC, Saito T, Averin S, Gissot S, et al. Developments, characterization and proton irradiation damage tests of AlN detectors for VUV solar observations. Nucl Instrum Meth B. 2013;312:48–53.

25. Zheng W, Lin R, Zhang D, Jia L, Ji X, Huang F. Vacuum-ultraviolet photovoltaic detector with improved response speed and responsivity via heating annihilation trap state mechanism. Adv Opt Mater. 2018;6:1800697.

26. Li T, Wang F, Lin R, Xie W, Li Y, Zheng W, et al. In-plane enhanced epitaxy for step-flow AlN yielding a high-performance vacuum-ultraviolet photovoltaic detector. CrystEngComm. 2020;22:654–9.

27. Jia L, Zheng W, Lin R, Huang F. Ultra-high photovoltage (2.45 V) forming in graphene heterojunction via quasi-fermi level splitting enhanced effect. iScience. 2020;23:100818.

28. Jia L, Li T, Huang F, Zheng W. Extremely high photovoltage (3.16 V) achieved in vacuum-ultraviolet-oriented van der Waals Photovoltaics. ACS Photonics. 2022;9:2101–8.

29. Jia L, Huang F, Zheng W. Vacuum ultraviolet (120–200 nm) avalanche photodetectors. Adv Opt Mater. 2022;10:2102424.

30. Shen GH, Liu Z, Zhang ML, Guo YF, Tang WH. 16×16 solar-blind UV detector based on β-Ga2O3 sensors. IEEE Electron Device Lett. 2023;44:1140–43.

31. Zhang Z, Lin C, Yang X, Zang J, Li K, Lu Y, et al. Wafer-sized polycrystalline diamond photodetector planar arrays for solar-blind imaging. J Mater Chem C. 2022;10:6488–96.

32. Zhou S, Zhang H, Peng X, Liu H, Li H, Xiong Y, et al. Fully transparent and high-performance ε-Ga2O3 photodetector arrays for solar-blind imaging and deep-ultraviolet communication. Adv Photon Res. 2022;3:2200192.

33. Barberini L, Cadeddu S, Caria M. A new material for imaging in the UV: CVD Diamond. Nucl Instrum Meth A. 2001;460:127–37.

34. Li R, Dong Y, Qian F, Xie Y, Chen X, Zhang Q, et al. CsPbBr3/graphene nanowall artificial optoelectronic synapses for controllable perceptual learning. PhotoniX. 2023;4:4.

35. Razeghi M, Rogalski A. Semiconductor ultraviolet detectors. J Appl Phys. 1996;79:7433–73.

36. Haboeck U, Siegle H, Hoffmann A, Thomsen C. Lattice dynamics in GaN and AlN probed with first- and second-order Raman spectroscopy. Phys Status Solidi (c). 2003;6:1710–31.

37. Goñi AR, Siegle H, Syassen K, Thomsen C, Wagner JM. Effect of pressure on optical phonon modes and transverse effective charges in GaN and AlN. Phys Rev B. 2001;64:035205.

38. Romijn J, Vollebregt S, Middelburg LM, Mansouri BE, Van Zeijl HW, May A, et al. Integrated 64 pixel UV image sensor and readout in a silicon carbide CMOS technology. Microsyst Nanoeng. 2022;8:114.

39. Yan T, Ge J, Su L, Liu X, Fang X. Designing ordered organic small-molecule domains for ultraviolet detection and micrometer-sized flexible imaging. Nano Lett. 2023;23:8295–302.

40. Du Y, Yin S, Li Y, Chen J, Shi D, Guo E, et al. Liquid-metal-assisted synthesis of patterned GaN thin films for high-performance UV photodetectors array. Small Methods. 2024;8:2300175.

41. Zhou S, Zheng Q, Yu C, Huang Z, Chen L, Zhang H, et al. A high-performance ε-Ga2O3-based deep-ultraviolet photodetector array for solar-blind imaging. Materials. 2022;16:295.

42. Wu W, Han X, Li J, Wang X, Zhang Y, Huo Z, et al. Ultrathin and conformable lead halide perovskite photodetector arrays for potential application in retina-like vision sensing. Adv Mater. 2021;33:2006006.

43. Huang C, He X. Easily processable Cu2O/Si self-powered photodetector array for image sensing applications. ACS Appl Electron Mater. 2022;4:1335–42.

44. Wu W, Wang X, Han X, Yang Z, Gao G, Zhang Y, et al. Flexible photodetector arrays based on patterned CH3NH3PbI3-xClx perovskite film for real-time photosensing and imaging. Adv Mater. 2019;31:1805913.

45. Chen Y, Fan X, Zhang Z, Miao G, Jiang H, Song H. AlGaN-based self-powered solar-blind UV focal plane array imaging photosensors: material growth, device preparation, and functional verification. IEEE Sens. J. 2023;23:20536–42.

46. Li Z, Li Z, Huang H, Yao Y, Khan B, Zhu Y, et al. Green lithium: photoelectrochemical extraction. PhotoniX. 2023;4:23.

47. Wang B, Mu J. High-speed Si-Ge avalanche photodiodes. PhotoniX. 2022;3:8.

48. Cai Q, You H, Guo H, Wang J, Liu B, Xie Z, et al. Progress on AlGaN-based solar-blind ultraviolet photodetectors and focal plane arrays. Light Sci Appl. 2021;10:94.

Publisher's Note